Electrocatalytic Hydrogen Evolution Over Micro and Mesoporous Cobalt Metal-Organic Frameworks

Bushra Iqbal[a], Andrea Laybourn[b], James N. O'Shea[c], Stephen P. Argent[d] and Muhammad Zaheer[a]*

[a]Department of Chemistry and Chemical Engineering, Syed Babar Ali School of Science and Engineering, Lahore University of Management Sciences (LUMS), Lahore 54792 Pakistan

[b]Advanced Materials Research Group, Faculty of Engineering, University of Nottingham, Nottingham, NG7 2RD, United Kingdom

[c]School of Physics and Astronomy, University of Nottingham, Nottingham NG7 2RD, United Kingdom

[d]School of Chemistry, University of Nottingham, Nottingham NG7 2RD, United Kingdom

*Corresponding author: muhammad.zaheer@lums.edu.pk

Abstract

The development of water electrolysis devices is crucial for the sustainable production of green hydrogen fuel. However, the slow kinetics and high overpotential are key shortfalls for hydrogen production during the half-cell hydrogen evolution reaction (HER) and significantly reduce the overall efficiency. Here we fabricated two micro- and mesoprorous cobalt MOFs $[Co(BDC)(DMSO)(DMF)]_n$ and $[Co(NH_2\text{-}BDC)(DMSO)(DMF)]_n$ (labeled Co-1 and Co-2, respectively) by using a benezenedicarboxylic acid (H_2BDC) linker and its amine-derivative (H_2N-BDC). The chemical functionalization of organic linkers in MOFs enhances catalytic activity by providing Lewis acidity or basicity, potentially enhancing electrocatalytic activity. Co-1 MOF ($[Co(BDC)(DMSO)]_n$) had a rod-like morphology, while Co-2 MOF ($[Co(NH_2\text{-}BDC)(DMSO)]_n$)

was in the form of two-dimensional sheets. After characterizing the materials using PXRD, SEM-EDX, XPS, TGA, FTIR, and gas sorption, we explored the electrocatalytic activity of the MOFs for hydrogen evolution reaction (HER). The presence of surface amino functions slightly improved HER activity of Cobalt MOFs in terms of overpotential (η from 0.217 V to 0.215 V @ 25mAcm^{2-}) and Tafel slope (from 95mVdec^{-1} to 91mVdec^{-1}). However, Co-2 showed better stability and high Faradic efficiency (97 %), which we attribute to morphological features, mesoporosity, and the presence of basic surface functionalities.

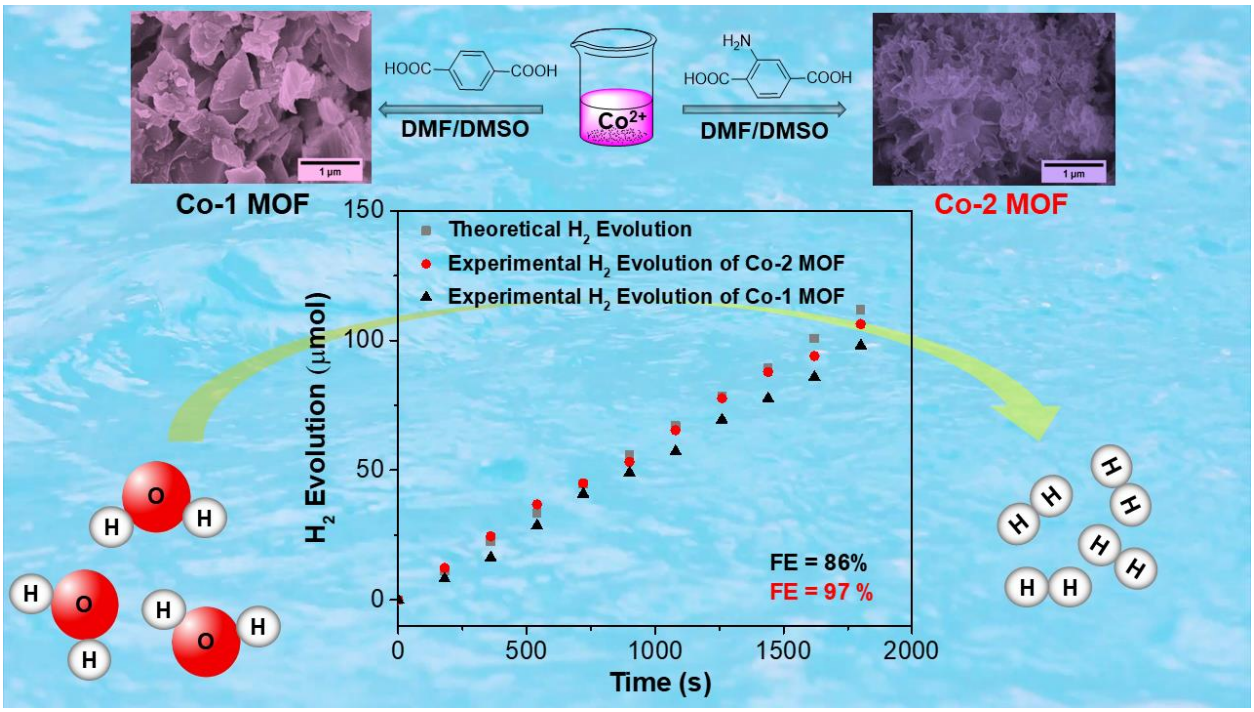

1. Introduction

The adverse effects of climate change due to the extensive use of fossil fuels have intensified the need for carbon-free renewable energy resources.[1] Hence, there is a great focus on developing efficient energy conversion systems which use hydrogen as an energy resource instead of fossil fuels. Water is an abundant and renewable source of hydrogen accessed via electrochemical water splitting.[2] Currently, hydrogen is exclusively produced from fossil resources and share of water electrolysis merely 4% [3], despite the latter being one of the most efficient, clean ways to produce hydrogen.[4] Hydrogen evolution reaction (HER) that takes place on the cathode of an electrochemical cell is one of the key steps of water splitting. Traditionally, noble metals and their compounds (e.g. Pt/C) are considered benchmark catalysts for HER due to their excellent electrochemical activities.[5, 6] However, high cost, unsatisfactory long-term stabilities, and inadequate resources (low abundancy *c.f.,* non-noble metals) limit their large-scale application and commercialization. Therefore, it is imperative to discover and develop efficient and economic electrocatalysts for HER based on non-noble metals based on both theory and experimentation.[7, 8]

Over the past few years, various kinds of electrocatalysts for HER have been reported, including metal carbides, nitrides,[9] chalcogenides,[10] oxides/hydroxides,[11] phosphides,[12] and alloys.[13] Current research focuses on developing earth-abundant metal electrocatalysts (mostly Fe, Co, Ni, W, Mn, Mo), which have received much interest due to their low toxicity, low cost, and excellent cost redox chemistry.[14] Cobalt-containing catalysts such as metallic cobalt, oxides, sulfides, and phosphides, have attracted attention for HER because of their incredible durability and electrical conductivity.[15, 16]

Metal-organic frameworks (MOFs) are promising catalytic materials due to their crystalline nature, high porosity, and versatile chemical composition.[17] However, electrocatalytic properties of three-dimensional MOFs are compromised due to poor electron mobility.[18] Various strategies have been used to improve the electrocatalytic activity of MOFs by making composites with conductive materials (*e.g.* Graphene),[19], and designing conductive MOFs [20] and carbon-based MOF derivatives for electrocatalytic water splitting.[21-23] Chemical modification of organic linkers is another way to enhance the electrocatalytic properties of MOFs. For instance, acidic and basic functional groups on the linkers mediate the catalytic property by electron-donating and withdrawing effects.[24, 25] Compared to pristine MOF-based OER catalysts, the discovery and development of HER electrocatalysts is a rapidly emerging research area. [26, 27] For instance, Dong and co-workers developed a 2D cobalt-containing MOF named THAT-Co for electrocatalytic HER using a mixture of thiol (THT) and amine (THA) based linkers. THAT-Co exhibited an overpotential of 283 mV at a current density of 10 $mAcm^{-2}$ and a Tafel slope of 71 $mVdec^{-1}$.[28] Wu *et al.* reported the electrocatalytic HER activity of two polymorphic Co-containing MOFs using a surfactant-assistant strategy (CTGU-5 and CTGU-6) in 0.5M H_2SO_4 electrolyte. The overpotential values of CTGU-5 and CTGU-6 were 388 and 425 mV, respectively.[29]

Inspired by the abovementioned examples, we investigated the solvothermal synthesis of two cobalt MOFs (Co-1 and Co-2) of different macroscopic morphologies using terephthalic acid and its NH_2 analog as organic linkers. The MOFs were then used as electrode materials for electrochemical HER activity, Faradic efficiency, and chronopotentiometric stability. Specifically, Co-2 showed relatively lower onset potential (0.15 V), low Tafel slope (91 mV/dec),

and high Faradic efficiency (97 %) in comparison to Co-1 and several reported MOF electrocatalysts such as NiCoO@CoNC[30] and Co@NC/NF.[31]

2. Experimental

2.1 Materials and Methods

Cobalt (II) nitrate hexahydrate, terephthalic acid (H_2BDC), 2-amino terephthalic acid (NH_2BDC), dimethylformamide (DMF), dimethyl sulfoxide (DMSO), and anhydrous ethanol were purchased from commercial suppliers (Sigma-Aldrich) and used as received.

2.2 Synthesis of Co-MOFs

The cobalt MOFs were prepared by a reported method.[32] For Co-1 MOF synthesis, $Co(NO_3)_2 \cdot 6H_2O$ (1 mmol) and H_2BDC (1 mmol) were separately dissolved in 5 mL DMF/DMSO (1:1 ratio) solvent. The cobalt solution was added dropwise into the linker solution while stirring to make the homogenous solution (total volume 10 mL). The clear solution was transferred to a 30 mL glass vial and heated at 120°C for 25 h in an oven. The resultant pink crystals were obtained by centrifugation, rinsed thoroughly with DMF (3x5 mL) and anhydrous ethanol (3x5 mL). After washing, the crystals were dried in a vacuum oven at 110°C for 12h. The same procedure was followed for Co-2 MOF; except H_2N-BDC linker was used instead of H_2BDC.

2.3 Characterizations

The phase purity and crystallinity of the samples were investigated via X-ray powder diffraction (P-XRD) with a BRUKER (D2 Phaser) diffractometer using CuKa irradiation (λ = 1.5406). SEM micrographs were taken using a scanning electron microscope (FEI NOVA Nano SEM 450) while

for elemental analysis, an energy-dispersive X-ray spectroscopy (EDS) detecto was used. The nitrogen physisorptio technique was employed for pososity and surface areas measurements using a Quantachrome Nova 2200e instrument. For FT-IR spectroscopy, a Bruker Alpha Platinum ATR spectrograph was used. Furthermore, thermogravimetric analysis was performed using a TA instrument (SDT Q600) from 25^{o}C to 700^{o}C (20 ^{o}C min^{-1} ramp) under an airflow (100 mL min^{-1}). X-ray photoelectron spectroscopy (XPS) was measured using a SPECS DeviSim near ambient pressure X-ray photoelectron spectroscopy (NAP-XPS) instrument incorporating an ultra-high vacuum (UHV) preparation/analysis chamber with Phoibos 150 NAP hemispherical analyzer. Monochromatic Al Kα X-rays (1486.6 eV) were used for all measurements, and the binding energy scale was calibrated using the main C-C C 1*s* component at 284.8 eV to compensate for steady-state charging in the semi-insulating samples. High-resolution spectra were curve-fitted using pseudo-Voigt lineshapes composed of a Lorentzian width determined by the core-hole lifetime and a Gaussian instrumental broadening, following subtraction of a Shirley or linear background as shown in the fit data.

2.4 Electrochemical Measurements

Electrocatalytic measurements were performed on a CH-instrument using a three-electrode setup. Cyclic voltammetry (CV) and linear sweep voltammetry (LSV) curves were taken at 50 mV/s scan rate in KOH (1M) and referenced against a reversible hydrogen electrode (RHE). MOF@Ni-foam, Hg/HgO and graphite rod were used as working, reference, and counter electrodes. Before use, Ni-foam was cleaned with HCl (1 M) in a sonication bath for 5 min to remove the surface oxides. The sample ink was prepared by mixing MOF (2 mg) and activated carbon (2 mg) in ethanol (200 μL) and Nafion solution (20 μl of 5 wt.%) via sonication. 50 μL of this slurry was deposited onto the

piece of Ni-foam (0.5 cm^2). To calculate the solution and charge transfer resistance, the electrochemical impedance spectroscopy (EIS) was acquired at an AC amplitude of 5 mV in 0.1 Hz –1.0 MHz frequency range. For double-layer capacitance (C_{dl}), polarization curves were taken at different scan rates (10-50 mV/s) in the non-Faradic region.

2.5 Calculation of electrochemical parameters

Electrochemical surface area (ECSA) and faradic efficiency were calculated using standard equations.[4]

$$E_{RHE} = E_{exp} + 0.0591 * pH + E_{Hg/HgO}\ (pH,\ 14\ for\ 1M\ KOH) \quad (1)$$

E_{RHE}, E_{exp} and $E_{Hg/HgO}$ refers to the potential of the reversible hydrogen electrode, experimental potential and reference electrode potential.

The overpotential was calculated using the following equation:

$$\eta = b \log j + a \quad (2)$$

η is the overpotential, b is the Tafel slope, and 'j' is the current density.

$$\text{Double layer charging current} = \nu\ Cdl \quad (3)$$

ν is the scan rate, and C_{dl} is the double layer capacitance equal to the slope of plot of 'ν' vs current density.

$$EASA = C_{dl}/C_s \quad (4)$$

C_s is the specific capacitance, and its value varies in the range of 0.02 - 0.13 mF/cm^2 in 1M KOH. The average value of 0.04 mF/cm^2 based on reported values was used herein.[6]

$$\text{Faradic efficiency} = \frac{z \times F \times n}{I \times t} \quad (5)$$

Z is the number of electrons transferred to produce 1 mole of H_2 ($2e^-$), F is the Faraday constant (96485.3 C/mol), n is the number of moles of hydrogen evolved, *I* refers to applied current *t* is the time.

The evolved gas was calculated via the water displacement method at 30 mAcm^{-2} during the amperostatic run.[33] An air-tight Bob cell was used to carry out the HER. The volume of evolved hydrogen gas was measured by a water burette and converted to moles of H_2 using ideal gas law.

3. Results & Discussion

The Co-MOFs were successfully synthesized by a solvothermal method using cobalt nitrate hexahydrate as the metal source and terephthalic acid (H_2BDC) or 2-aminoterephthalic acid (H_2NBDC) as ligands in a mixed solvent system (DMF:DMSO) as presented in Figure 1. Co-1 MOF was obtained as light pink crystals, while Co-2 MOF was a purple powder upon drying.

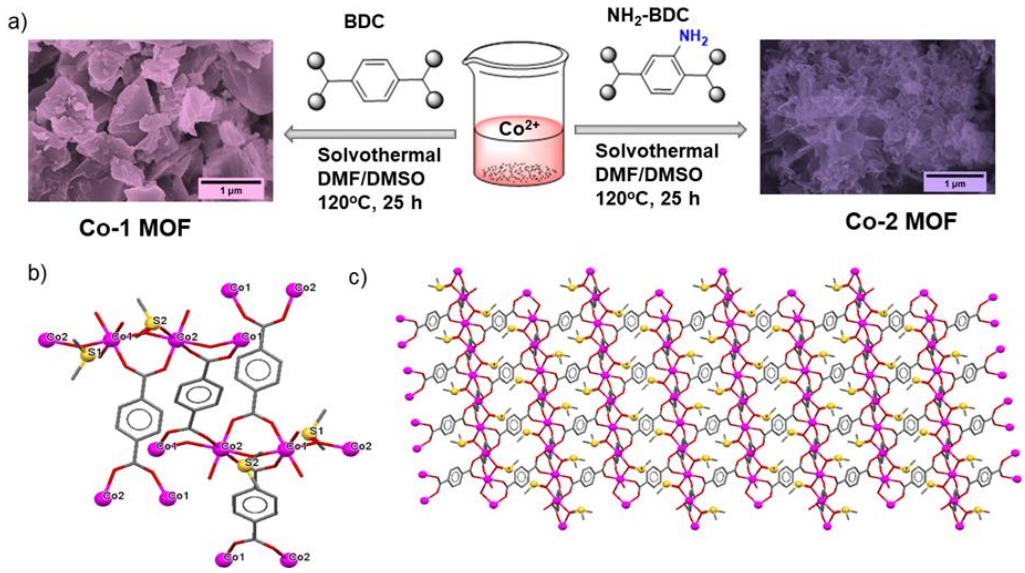

Figure 1 a) Synthesis scheme of Co-MOFs. X-ray Crystal structure of reported r-MOF (rod-shape MOF).[34] b) SBU of Co-O chain, c) 3D network of r-MOF. Colour scheme: Co, pink; C, grey; O, red; S, yellow. H atoms are omitted for clarity.

A selection of pink block-like single crystals of Co-1 MOF were examined by single-crystal X-ray diffraction (SCXRD) and determined to have triclinic unit cells with the dimensions a = 7.2725(1) Å, b = 10.8716(2) Å, c = 15.8397(3), a = 72.423(2)°, b = 79.173(2)°, g = 73.860(2). These unit cell dimensions match CSD entry 1000296 (LOMQOV) catena-[tetrakis(m4-Terephthalato)-tetrakis(dimethyl sulfoxide)-tetra-cobalt] reported as r-MOF (r: rod-shaped) in the literature. [34] We, therefore, simulated the Powder X-ray Diffraction (PXRD) pattern from SCXRD data of r-MOF (CCDC:1000296) and compared it with PXRD patterns of Co-1 and Co-2. As shown in Figure 2a, the PXRD pattern of Co-1 and Co-2 matches nicely with r-MOF. The sharp peaks in the diffraction pattern of Co-1 correspond to greater crystallinity than Co-2, which showed broader peaks of low intensity indicative of smaller crystalline domains and structural changes. Compared to the simulated pattern, a slight peak shift was observed at 25° (2θ), which might be due to the breathing phenomenon [35] due to the flexible crystal structure of the MOFs.

MOF-71, another Co-based MOF with the same building blocks (Co(ii) ions and BDC linker), has an entirely different crystal structure.

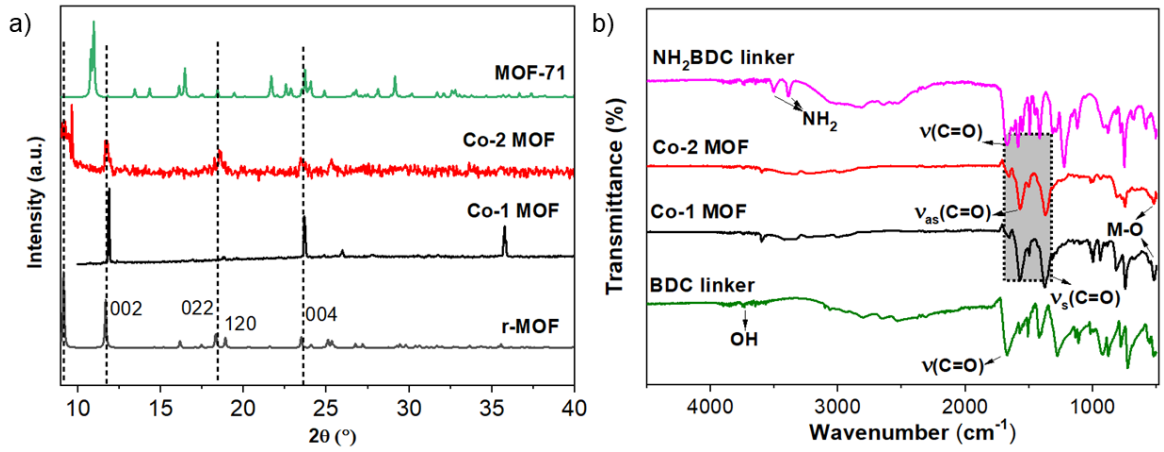

Figure 2 a) PXRD patterns and b) FT-IR spectra of Co-MOFs

The crystal structure of both MOFs (Figure 1b) contains two crystallographically unique cobalt atoms (Co1 and Co2), each coordinated to six oxygen atoms, of which the BDC linker provides four while DMSO/DMF solvent molecules offer two. Both Co-1 and Co-2 MOFs also have connected DMSO molecules. The Co chains extend via BDC linkers to form a three-dimensional network. The empirical formulae $[Co(BDC)(DMSO)(DMF)]_n$ and $[Co(NH_2\text{-}BDC)(DMSO)(DMF)]_n$, for Co-1 and Co-2, respectively, were confirmed by EDX analysis, and we found a close agreement between theoretical and experimental elemental composition (Table S1).

Fourier Transform Infrared (FT-IR) spectra of the Co-MOFs and the corresponding linkers are shown in Figure 2b. In both materials, characteristic bands for anti-symmetric and symmetric vibrations of coordinated carboxylate C-O were observed at 1570 and 1370 cm^{-1}.[36] The disappearance of the peak at 1679 cm^{-1} verifies the absence of the unreacted linker.[37, 38] Both

Co-1 and Co-2 also have coordinated DMSO, as evident from small peaks around 862-997 cm^{-1}. The presence of S in synthesized MOFs was also evidenced by EDX and XPS analysis discussed later. The presence of uncoordinated DMSO was ruled out due to the absence of bands at 1005 cm^{-1}.[39] Metal bonded oxygen (M-O) appeared in the region of 400 to 800 cm^{1}.

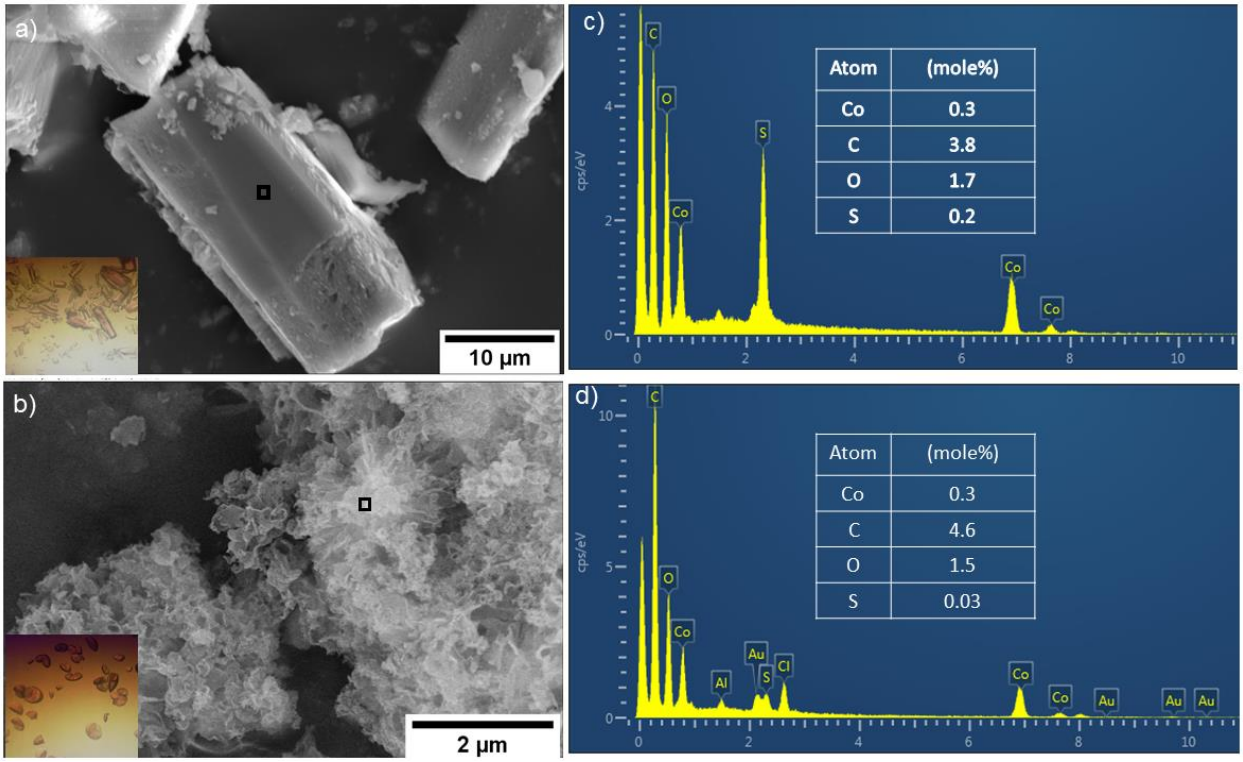

Figure 3. a-b) SEM images) and c-d) EDX spectra of Co-1 and Co-2 MOFs. The insets in (a) and (b) show light microscopic images of Co-1 and Co-2, respectively. The elemental composition of Co-1 and Co-2 is presented as tables in Figures (c) and (d), respectively.

The surface morphology and elemental composition of the Co-MOFs were determined by Scanning Electron Microscopy (SEM) and Energy-Dispersive X-ray Spectroscopy (EDX), respectively. Both under a light microscope (inset Figure 3a) and SEM (Figure 3a), Co-1 exhibited a rod-like morphology as reported in the literature for r-MOF. However, Co-2 morphology differed from r-MOF (rods) and MOF-71 (cubes) and consisted of two-dimensional sheets folded and

arranged in a flower-like structure as presented in the SEM image (Figure 3b) and light microscopic image (inset in Figure 3b).

Elemental analysis (Figures 3c-d and inset tables) demonstrated a relatively uniform distribution of Co, C, O, and S elements in both MOFs with a comparable Co concentration. The amount of sulfur, however, in Co-2 (Figure 3d) was found to be much lower, which might be due to the electronic and steric effects of the amino group at the benzene ring, which discourage the binding of DMSO with the metal center.

Thermogravimetric analyses were performed in the air to check the thermal stability Co-1 and Co-2, and decomposition profiles are presented in Figure 4a. A 25.6% and 24.2% weight loss at 250-350°C was observed for Co-1 and Co-2, respectively, corresponding to the removal of coordinated solvent molecules (calculated 25.9%). The loss of linker molecules was observed above 350°C with a mass loss of 49.3% for Co-1 and 46 % for Co-2**,** respectively. Both MOFs' TGA curves were similar to the reported r-MOF. Co-1 exhibited rapid weight loss after 300°C, implying faster decomposition than Co-2, which showed multistep deterioration. The calculations for mass loss of coordinated solvent and linkers suggested the ($[Co(BDC)(DMSO)(DMF)]_n$) and ($[Co(NH_2\text{-}BDC)(DMSO)(DMF)]_n$) empirical formulas for Co-1 and Co-2, respectively.

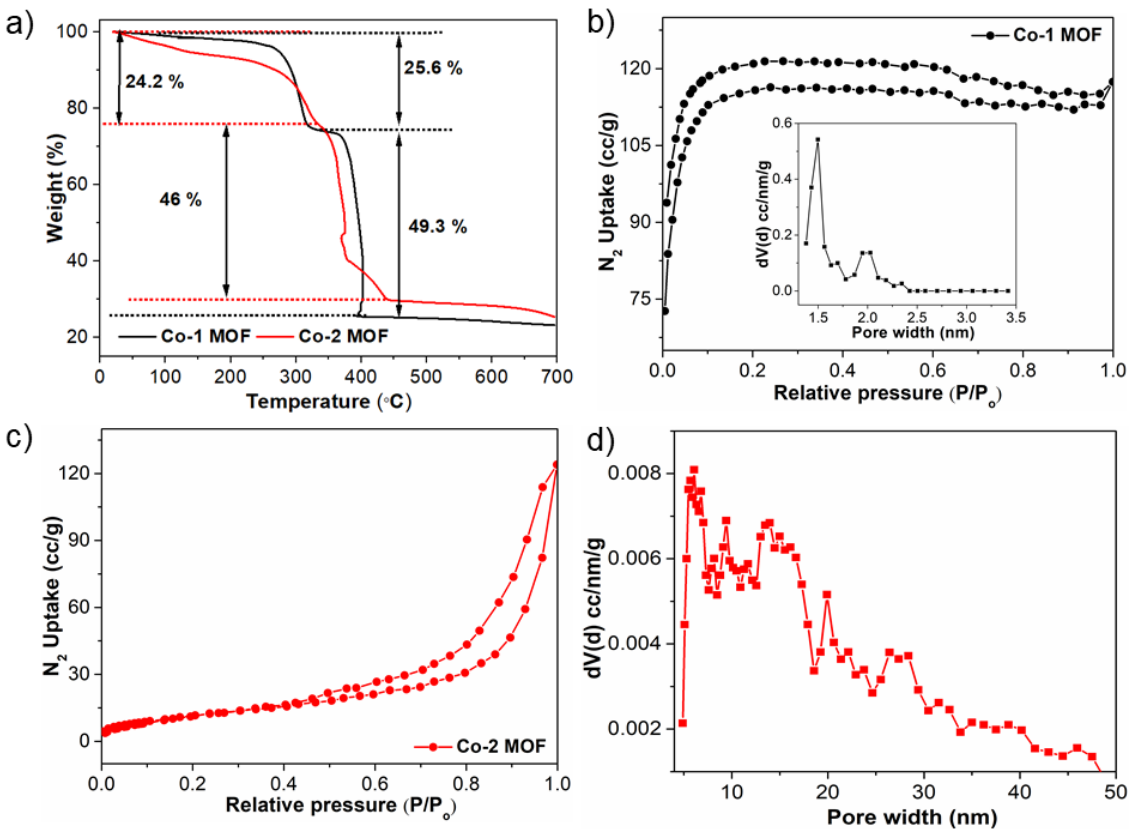

Figure 4. a) TGA thermogram, b) N_2 adsorption-desorption isotherm (pore size distribution, inset) of Co-1 MOF. c) N_2 adsorption-desorption isotherm and d) pore size distribution of Co-2 MOF

The porosity of Co-1 and Co-2 was determined by nitrogen physisorption at 77 K. High nitrogen uptake at low relative pressure (P/P_0) and type-I adsorption isotherm suggested microporosity in Co-1 MOF (Figure 4b). Pore size distribution (Inset Figure 4b) calculated via the Non-local Density Functional Theory (NLDFT) model provided an average pore diameter of 1.5 nm, which also supports the microporous nature of Co-1. The material exhibited a BET surface area of 449 m^2/g, with a pore volume of 0.18 cm^3/g. Interestingly, Co-2 showed a Type-IV isotherm with hysteresis loop closing at $P/P_0 = 0.4$, indicating mesoporosity with an average 6 nm pores (Figures 4c-d). However, the BET surface area was relatively low (32 m^2/g) but showed a similar pore

volume (0.17 cm^3/g,) compared to Co-1. The decrease in BET surface area of Co-2 is possibly due to the presence of -NH_2 groups of the aminated linker, as reported in the literature.[40]

Co-1 and Co-2 were also analyzed with X-ray photoelectron spectroscopy (XPS) to verify the oxidation state of cobalt and their coordination environment and elemental composition of the MOFs. The survey scan showed the presence of C, N, O, S, and Co as recognized by their typical binding energies in both Co-1 and Co-2 (Figure 5a). The XPS elemental composition for both MOFs is almost consistent with the EDX measurement and is given in table S1 (supporting information). The high-resolution carbon (1s) spectrum (Figure 5b) has been fitted to three components at 284.8, 286.1, and 288.4 eV, corresponding to C=C, C-O, and C=O bonds. The broad component on the low binding energy side is attributed to the supporting graphite pad (overcompensated by the flood gun). The of O 1s spectrum was fitted to three components, i.e., metal-oxygen bond (peak at 529.6 eV), weak oxygen coordination (at 530.4 eV), and oxygen contribution from surface adsorbed water (at 531.5 eV) (Figure 5c).

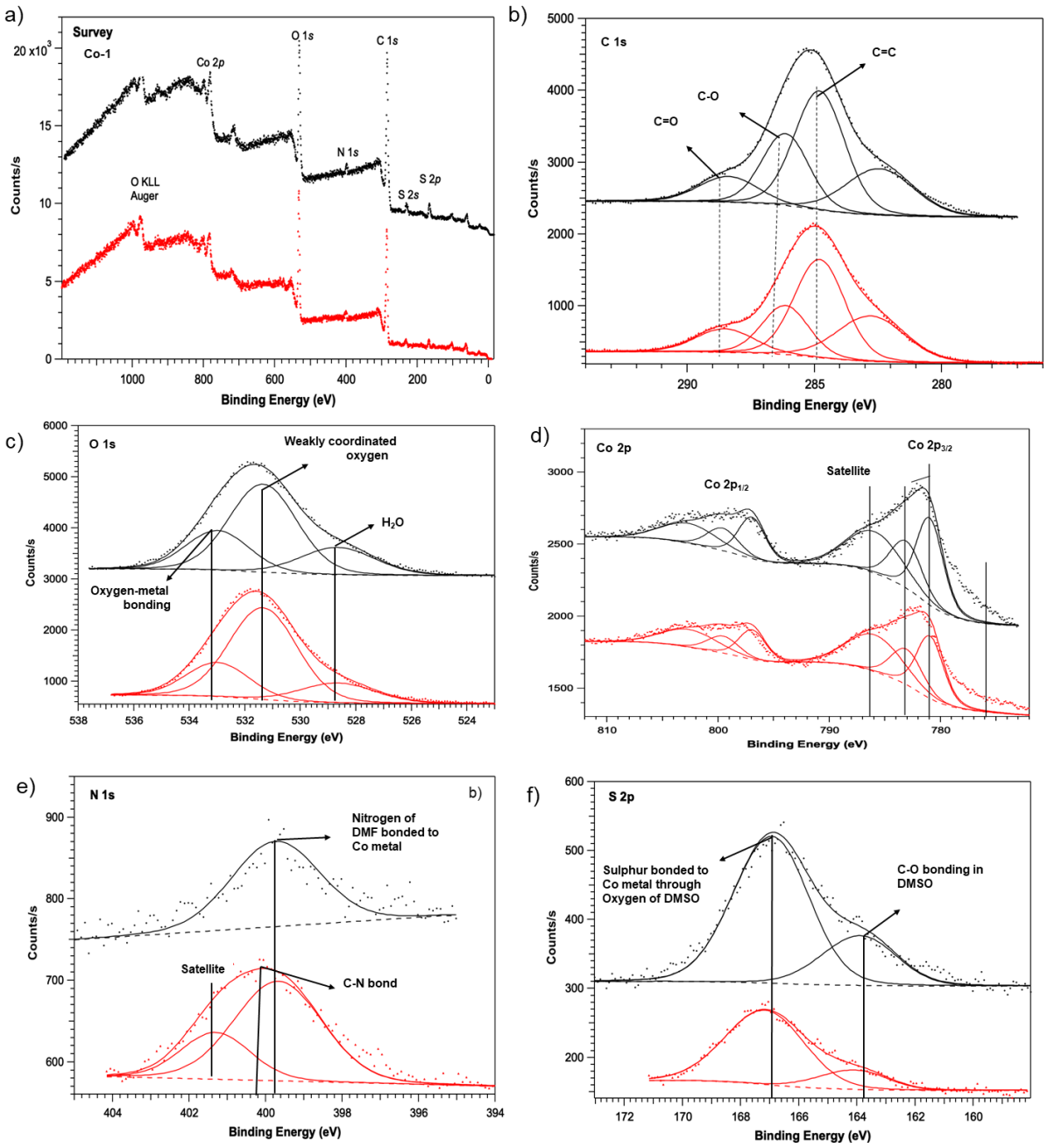

Figure 5. XPS analysis of Co-MOFs. a) elemental survey, b) C 1s, c) O 1s, d) Co 2p, e) N 1s and f) S 2p spectra

The Co 2p high-resolution spectrum (Figure 5d) consisted of two peaks at binding energies of 782.0 and 795.5eV for Co $2p_{3/2}$ and Co $2p_{1/2}$, respectively. The presence of two pronounced satellite peaks (786 eV and 803.11 eV) demonstrates that Co ions are predominantly in the Co^{2+} state in both MOFs.[41] The nitrogen 1s peak in Co-2 is curve-fitted to two peaks centered at 399.5 and

401.2 eV, which we attribute to the metal-nitrogen bonding and amine bonding, respectively (Figure 6e).[42] Nitrogen is also detected in Co-1 due to coordinated DMF in the structure, as also evident from EDX data. The S2p spectrum has been curve-fitted using two lineshapes, each comprising both the $S2p_{3/2}$ and $Sp_{1/2}$ components with a spin-obrit splitting of 1.2 eV and a branching ratio of 2. The two contributions indicate two chemical environments for the sulfur atom. The high binding energy peak centred around 167 eV is attributed to S bonded to the Co through the oxygen of the DMSO molecule, while the peak 3 eV to lower binding energy we attribute to C-S bonding in DMSO molecules.[43]

The HER catalytic performances of Co-1 and Co-2 modified Nickel foam electrodes were studied in 1M KOH (electrolyte) using a three-electrode setup. The linear sweep voltammograms (LSVs) were initially recorded for Co-1 and Co-2 by applying negative potentials. According to the LSV curves in Figure 6a, the Co-2/NF (NF = Nickel Foam) demonstrated an overpotential of 215 mV at a current density of 25 mA/cm^2, which is much lower than AC/NF (Activated Carbon, 248 mV), nickel foam (without catalyst, 262 mV) and comparable to Co-1/NF (217 mV) and the state-of-the-art Pt/C catalyst.

The Co-2 electrode exhibited promising HER kinetics with a Tafel slope of 91 mV/dec, lower than that of Co-1 (95 mV/dec), Pt/C (63 mV/dec), AC (139 mV/dec) and bare Ni-foam (245 mV/dec) (Figure 6b). The smaller Tafel slope justifies hydrogen adsorption as the rate-determining step (RDS) via a Volmer-Heyrovsky mechanism.[44] and surface $–NH_2$ functions seem to facilitate this process. Due to active cobalt sites, water dissociation is promoted and H is adsorbed at the catalyst's surface. The nitrogens of the amine group further facilitate the Hyrovsky step, and the hydrogen produced via water dissociation combines with adsorbed hydrogen to form molecular

hydrogen (Figure S1). The synergistic effect of the cobalt and amine group, therefore, enhances the HER performance of Co-2 MOF compared to Co-1 (supporting information).

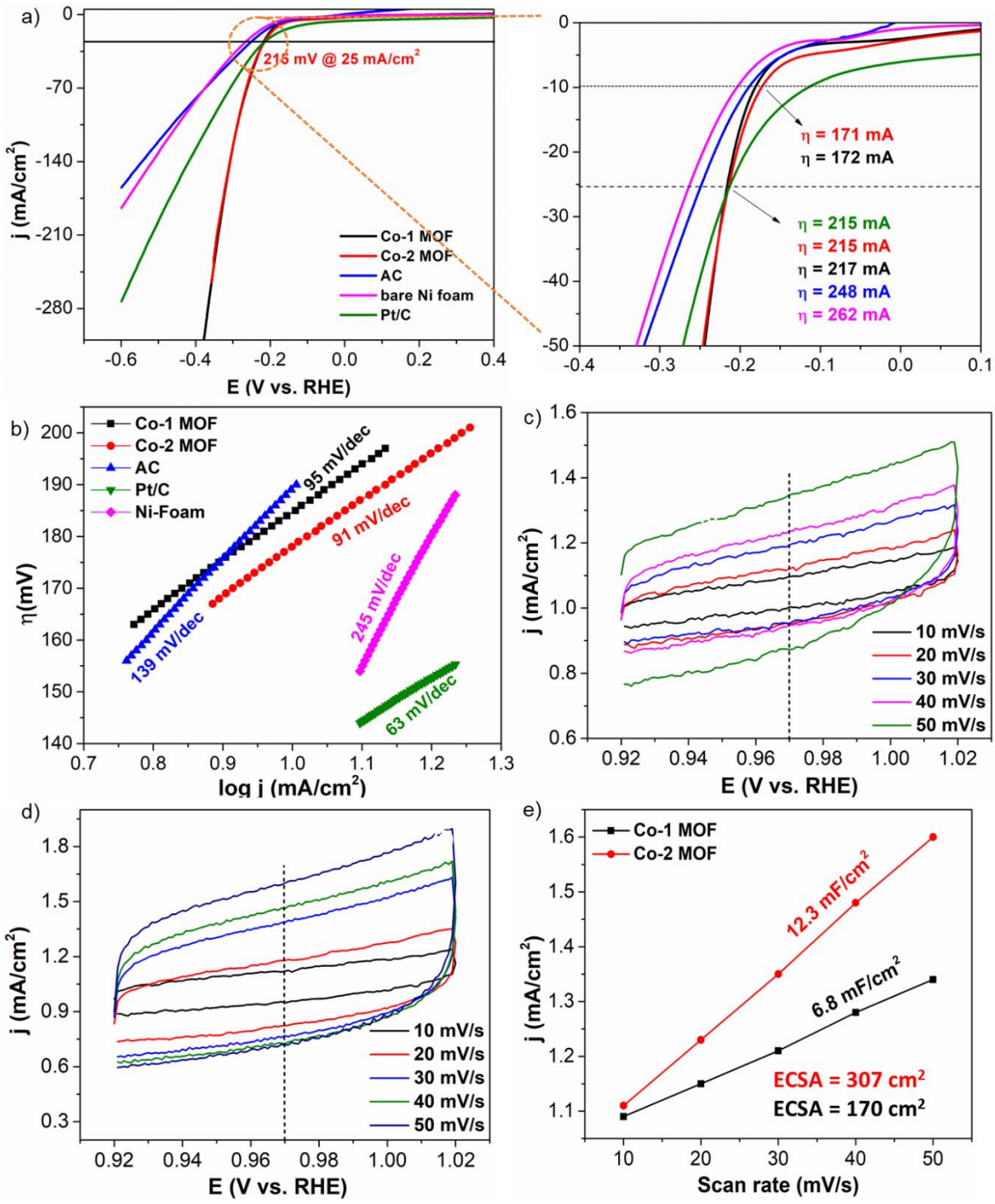

Figure 6 a) LSV measurements in the negative potential range for HER iR correction, b) Tafel slopes for the corresponding samples. CV curves of c) Co-1 MOF and d) Co-2 MOF at different scan rates from 10 to 50 mV/s, e) Electrochemical double-layer capacitances of Co-MOFs

The double-layer capacitance (C_{dl}) was measured in the non-Faradic region via cyclic voltammetry to calculate the electrochemically active surface area (EASA). The CVs at different scan rates in

non-Faradic region Co-1 and Co-2 are presented in Figures 6c and 6d, respectively. For both catalysts, an increase in current density was observed upon increasing the scan rate; however, higher current density in the case of Co-2 nanosheets indicated a higher number of exposed active sites. Also, the EASA (see Table 1) for Co-2 was found to be 307 cm^2 which is more than twice the surface area of Co-1 (170 cm^2). Both high current response and high active surface area indicate the potential of Co-2 as a suitable HER catalyst.

Moreover, the kinetics of the HER process was evaluated from the electrochemical impedance spectroscopy (EIS) in terms of charge transfer. The relative Nyquist plots for the three-electrode system are shown in Figure 7a. The Rct values for Co-MOFs were measured from the diameter of the semicircle and Rs values from the initial point of the semicircle in the Nyquist plots (at the low-frequency region). The charge transfer resistance (Rct) and solution resistance (Rs) values obtained from the Nyquist plot indicated the negative influence of the electrode and solution resistance on the activity of the catalyst. The smaller Rct (16.4 Ω), smaller Tafel slope and high EASA for Co-2 compared to Co-1 justifies its slightly higher activity. The electrochemical parameters are listed in Table 1.

Table 1 Comparison of the EASA and HER performance of cobalt catalysts. Values are for material measured herein.

Samples	EASA (cm^2)	η25 for HER (mV)	Tafel Slope HER ($mVdec^{-1}$)	Rct (Ω)	Rs (Ω)
Co-1	170	217	95	20.8	3.8
Co-2	307	215	91	16.3	2.8

AC	-	248	139	41	2.0
Pt/C	-	215	63	5.9	2.7
Ni-Foam		262	245	-	2.7

[a] η, overpotential; EASA, electrochemical active surface area; Rs, solution resistance; Rct, charge transfer resistance

The stability of the Co-2 MOF catalyst was tested by running a chronopotentiometry scan for 20 hours (Figure 7b). The catalysts showed decent stability, and slight variation in overpotential over time might be caused by the bubble formation on the surface of Ni-foam as the experiments were performed under static conditions

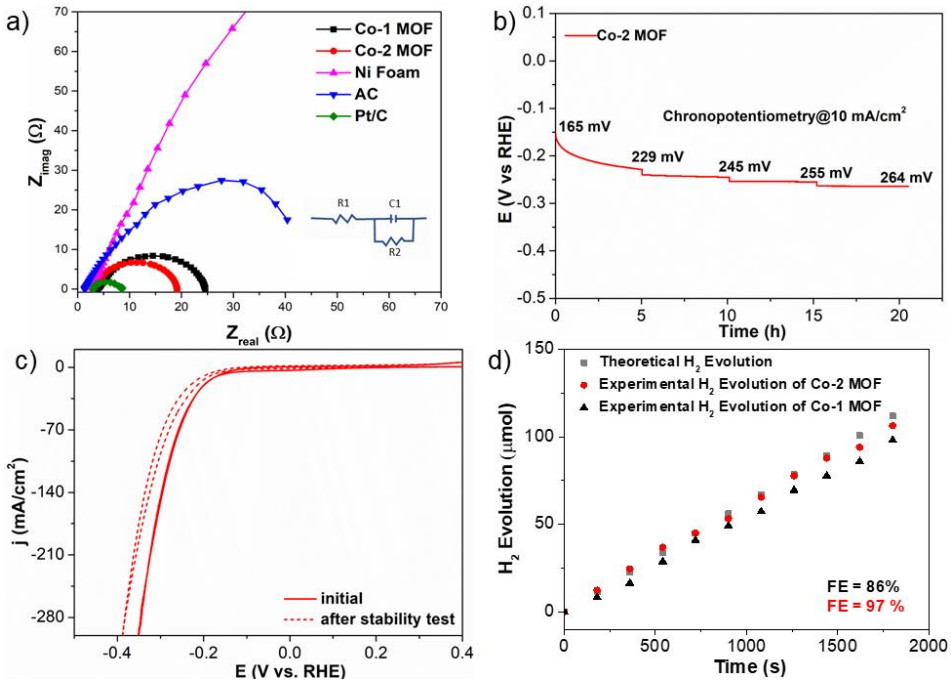

Figure 7. a) Nyquist plots of Co-1 and Co-2 (inset shows circuit diagram). b) Chronopotentiometric stability curve to maintain a current density of 10mA/cm^2. c) CV measurements (without iR-correction) before and after the stability test for 20 hours and d) Comparison of theoretically calculated hydrogen evolution with experimental one.

The polarization curves for the Co-2 electrode before and after the stability test, showed only a slight deactivation (Figure 7c).

Furthermore, quantitative analysis for molecular hydrogen was performed to check the selectivity of the catalysts. The released H_2 gas was computed by the water displacement method [33] at 200 mA/cm^2 current density for 30 minutes. The Faradic efficiency (FE) was calculated by comparing the experimental and theoretical amounts of evolved hydrogen gas at regular time intervals (Figure 7d). Co-2 showed a better FE (97%) compared to Co-1 (86 %).

For comparison, the stability test was also conducted for one h at 10 mA/cm^2 using Co-1 and Co-2, during which the catalysts showed minor changes in overpotential (Figure 8). However, a change in morphological features of the catalysts was observed in SEM analysis after the catalysis. For instance, the 2D sheets of Co-2 MOF degraded and changed into hexagonal and polyhedral disk-like structures (Figure S2 from supporting information).

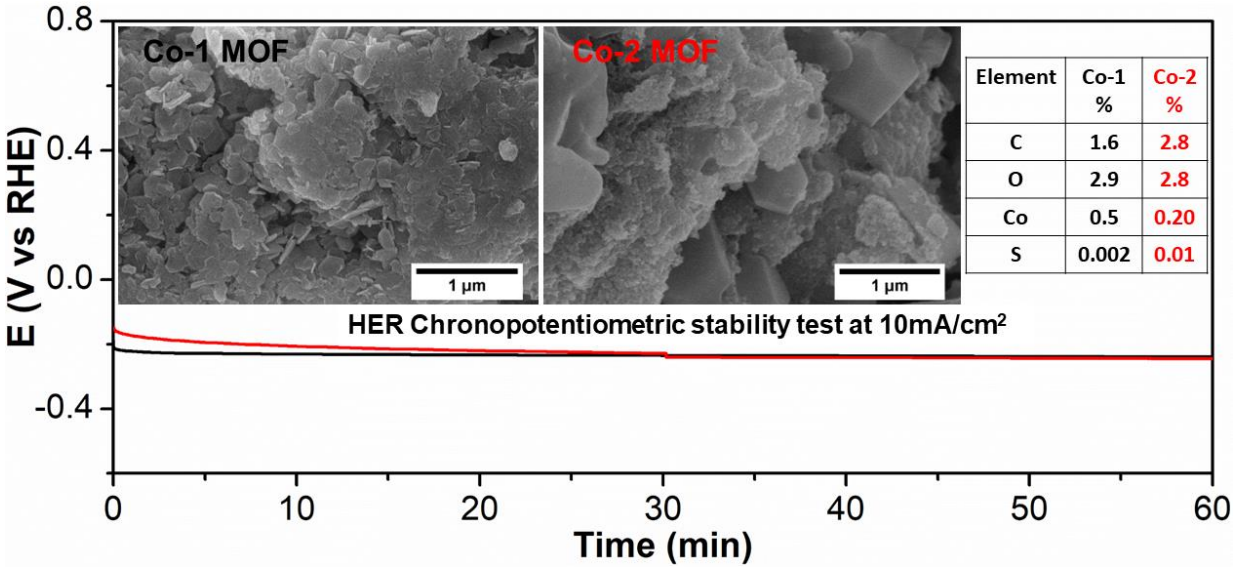

Figure 8 Chronopotentiometry test along with SEM images of Co-1 and Co-2 MOF after one h stability test.

Insets show SEM images and EDX of the catalysts after HER.

The HER activity of Co-1 ad Co-2 is higher than many previously reported MOFs and MOF-derived catalysts (Table S2 in supporting information).

4. Conclusion

In summary, the electrochemical performance of two morphologically different Co-MOFs (Co-1 and Co-2) were evaluated for the hydrogen evolution reaction in an alkaline medium. The microscopic analysis indicated that microporous Co-1 possessed a three-dimensional rod-like morphology, while aminated mesoporous Co-2 showed a flower-like two-dimensional structure. Co-1 and Co-2 catalyze the HER process at comparable overpotentials (0.172 V and 0.171 V@10mAcm^{2-}) and kinetics (Tafel slope: 95 mV/dec and 91 mV/dec), respectively, which is comparable to the state-of-the-art 1 wt.% Pt/C catalyst. However, Co-2 provided better Faraday efficiency and stability for up to twenty hours. The findings reveal the potential of MOF-based electrocatalysts based on earth-abundant metal for renewable hydrogen generation from water.

Acknowledgments

M.Z. thanks the Higher Education Commission (HEC) of Pakistan for financial support under a National Research Program for Universities (NRPU grants # 4130 and 5910). B.I. acknowledges the HEC for sponsoring a short-term stay at the University of Nottingham under IRSIP program. SEM and TEM analyses in this work were supported by the Engineering and Physical Sciences Research Council (EPSRC) [under grant EP/L022494/1] and the University of Nottingham. The authors thank the Nanoscale and Microscale Research Centre (nmRC) for providing access to instrumentation and Grace Belshaw, Nicola Weston, and Michael Fay for technical assistance.

Declaration of competing interest

The authors declare that they have no known competing financial interests or personal relationships that could have appeared to influence the work reported in this paper.

CRediT Author Statement

Bushra Iqbal: Investigation, writing-original draft. **Andrea Laybourn**: supervision, resources, writing review & editing. **James O'Shea:** XPS data collection, curve fitting, and interpretation. **Stephen Argent:** Crystallography. **Muhammad Zaheer**: conceptualization, supervision, project administration, funding acquisition, writing-review & editing

References

[1] W. Leitner, E.A. Quadrelli, R. Schlögl, Harvesting renewable energy with chemistry, Green Chemistry, 19 (2017) 2307-2308.
[2] S. Penner, Steps toward the hydrogen economy, Energy, 31 (2006) 33-43.
[3] M. Balat, Potential importance of hydrogen as a future solution to environmental and transportation problems, International journal of hydrogen energy, 33 (2008) 4013-4029.
[4] X. Li, X. Hao, A. Abudula, G. Guan, Nanostructured catalysts for electrochemical water splitting: current state and prospects, Journal of Materials Chemistry A, 4 (2016) 11973-12000.
[5] R. Jana, C. Chowdhury, S. Malik, A. Datta, Pt/Co3O4 Surpasses Benchmark Pt/C: An Approach Toward Next Generation Hydrogen Evolution Electrocatalyst, ACS Applied Energy Materials, 2 (2019) 5613-5621.
[6] C.C. McCrory, S. Jung, J.C. Peters, T.F. Jaramillo, Benchmarking heterogeneous electrocatalysts for the oxygen evolution reaction, Journal of the American Chemical Society, 135 (2013) 16977-16987.
[7] W. Seh Zhi, J. Kibsgaard, F. Dickens Colin, I. Chorkendorff, K. Nørskov Jens, F. Jaramillo Thomas, Combining theory and experiment in electrocatalysis: Insights into materials design, Science, 355 (2017) eaad4998.
[8] J. Resasco, F. Abild-Pedersen, C. Hahn, Z. Bao, M.T.M. Koper, T.F. Jaramillo, Enhancing the connection between computation and experiments in electrocatalysis, Nature Catalysis, 5 (2022) 374-381.
[9] W.-F. Chen, J.T. Muckerman, E. Fujita, Recent developments in transition metal carbides and nitrides as hydrogen evolution electrocatalysts, Chemical communications, 49 (2013) 8896-8909.

[10] J. McAllister, N.A. Bandeira, J.C. McGlynn, A.Y. Ganin, Y.-F. Song, C. Bo, H.N. Miras, Tuning and mechanistic insights of metal chalcogenide molecular catalysts for the hydrogen-evolution reaction, Nature communications, 10 (2019) 1-10.
[11] N. Danilovic, R. Subbaraman, D. Strmcnik, K.C. Chang, A. Paulikas, V. Stamenkovic, N.M. Markovic, Enhancing the alkaline hydrogen evolution reaction activity through the bifunctionality of Ni (OH) 2/metal catalysts, Angewandte Chemie, 124 (2012) 12663-12666.
[12] J.F. Callejas, C.G. Read, C.W. Roske, N.S. Lewis, R.E. Schaak, Synthesis, characterization, and properties of metal phosphide catalysts for the hydrogen-evolution reaction, Chemistry of Materials, 28 (2016) 6017-6044.
[13] G. Lu, P. Evans, G. Zangari, Electrocatalytic properties of Ni-based alloys toward hydrogen evolution reaction in acid media, Journal of the Electrochemical Society, 150 (2003) A551.
[14] Z. Chen, X. Duan, W. Wei, S. Wang, B.-J. Ni, Recent advances in transition metal-based electrocatalysts for alkaline hydrogen evolution, Journal of Materials Chemistry A, 7 (2019) 14971-15005.
[15] H. Zhong, C.A. Campos-Roldán, Y. Zhao, S. Zhang, Y. Feng, N. Alonso-Vante, Recent advances of cobalt-based electrocatalysts for oxygen electrode reactions and hydrogen evolution reaction, Catalysts, 8 (2018) 559.
[16] W. Han, M. Li, Y. Ma, J. Yang, Cobalt-based metal-organic frameworks and their derivatives for hydrogen evolution reaction, Frontiers in Chemistry, 8 (2020) 1025.
[17] H. Furukawa, K.E. Cordova, M. O'Keeffe, O.M. Yaghi, The chemistry and applications of metal-organic frameworks, Science, 341 (2013).
[18] M.A. Nasalevich, M. van der Veen, F. Kapteijn, J. Gascon, Metal–organic frameworks as heterogeneous photocatalysts: advantages and challenges, CrystEngComm, 16 (2014) 4919-4926.
[19] L.G. Beka, X. Bu, X. Li, X. Wang, C. Han, W. Liu, A 2D metal–organic framework/reduced graphene oxide heterostructure for supercapacitor application, RSC advances, 9 (2019) 36123-36135.
[20] L.S. Xie, G. Skorupskii, M. Dincă, Electrically Conductive Metal–Organic Frameworks, Chem. Rev., 120 (2020) 8536-8580.
[21] H.-F. Wang, L. Chen, H. Pang, S. Kaskel, Q. Xu, MOF-derived electrocatalysts for oxygen reduction, oxygen evolution and hydrogen evolution reactions, Chem. Soc. Rev., 49 (2020) 1414-1448.
[22] J. Liu, D. Zhu, C. Guo, A. Vasileff, S.-Z. Qiao, Design Strategies toward Advanced MOF-Derived Electrocatalysts for Energy-Conversion Reactions, Advanced Energy Materials, 7 (2017) 1700518.
[23] B. Zhu, R. Zou, Q. Xu, Metal–organic framework based catalysts for hydrogen evolution, Advanced Energy Materials, 8 (2018) 1801193.
[24] W. Zheng, L.Y.S. Lee, Metal–organic frameworks for electrocatalysis: catalyst or precatalyst?, ACS Energy Letters, 6 (2021) 2838-2843.
[25] K. Chakarova, I. Strauss, M. Mihaylov, N. Drenchev, K. Hadjiivanov, Evolution of acid and basic sites in UiO-66 and UiO-66-NH2 metal-organic frameworks: FTIR study by probe molecules, Microporous and Mesoporous Materials, 281 (2019) 110-122.
[26] D.S. Raja, H.-w. Lin, S.-y. Lu, Nano Energy Synergistically well-mixed MOFs grown on nickel foam as highly e ffi cient durable bifunctional electrocatalysts for overall water splitting at high current densities, Nano Energy, 57 (2019) 1-13.

[27] J.Y. Xue, C. Li, F.L. Li, H.W. Gu, P. Braunstein, J.P. Lang, Recent advances in pristine tri-metallic metal-organic frameworks toward the oxygen evolution reaction, Nanoscale, 12 (2020) 4816-4825.
[28] R. Dong, Z. Zheng, D.C. Tranca, J. Zhang, N. Chandrasekhar, S. Liu, X. Zhuang, G. Seifert, X. Feng, Immobilizing molecular metal dithiolene–diamine complexes on 2D metal–organic frameworks for electrocatalytic H2 production, Chemistry–A European Journal, 23 (2017) 2255-2260.
[29] Y.P. Wu, W. Zhou, J. Zhao, W.W. Dong, Y.Q. Lan, D.S. Li, C. Sun, X. Bu, Surfactant-Assisted Phase-Selective Synthesis of New Cobalt MOFs and Their Efficient Electrocatalytic Hydrogen Evolution Reaction, Angewandte Chemie, 129 (2017) 13181-13185.
[30] G. Cai, W. Zhang, L. Jiao, S.-H. Yu, H.-L. Jiang, Template-directed growth of well-aligned MOF arrays and derived self-supporting electrodes for water splitting, Chem, 2 (2017) 791-802.
[31] A. Aijaz, J. Masa, C. Rösler, W. Xia, P. Weide, R.A. Fischer, W. Schuhmann, M. Muhler, Metal–organic framework derived carbon nanotube grafted cobalt/carbon polyhedra grown on nickel foam: an efficient 3D electrode for full water splitting, ChemElectroChem, 4 (2017) 188-193.
[32] Q. Wang, C. Wei, D. Li, W. Guo, D. Zhong, Q. Zhao, FeNi-based bimetallic MIL-101 directly applicable as an efficient electrocatalyst for oxygen evolution reaction, Microporous and Mesoporous Materials, 286 (2019) 92-97.
[33] Y. Hu, Z. Wang, W. Liu, L. Xu, M. Guan, Y. Huang, Y. Zhao, J. Bao, H.-m. Li, Novel cobalt–iron–vanadium layered double hydroxide nanosheet arrays for superior water oxidation performance, ACS Sustainable Chemistry & Engineering, 7 (2019) 16828-16834.
[34] K.J. Lee, T.-H. Kim, T.K. Kim, J.H. Lee, H.-K. Song, H.R. Moon, Preparation of Co 3 O 4 electrode materials with different microstructures via pseudomorphic conversion of Co-based metal–organic frameworks, Journal of Materials Chemistry A, 2 (2014) 14393-14400.
[35] C. Mellot-Draznieks, C. Serre, S. Surblé, N. Audebrand, G. Férey, Very large swelling in hybrid frameworks: a combined computational and powder diffraction study, Journal of the American Chemical Society, 127 (2005) 16273-16278.
[36] Z.-L. Huang, M. Drillon, N. Masciocchi, A. Sironi, J.-T. Zhao, P. Rabu, P. Panissod, Ab-Initio XRPD Crystal Structure and Giant Hysteretic Effect (H c= 5.9 T) of a New Hybrid Terephthalate-Based Cobalt (II) Magnet, Chemistry of materials, 12 (2000) 2805-2812.
[37] B. Wu, X. Lin, L. Ge, L. Wu, T. Xu, A novel route for preparing highly proton conductive membrane materials with metal-organic frameworks, Chemical Communications, 49 (2013) 143-145.
[38] H. Embrechts, M. Kriesten, M. Ermer, W. Peukert, M. Hartmann, M. Distaso, In situ Raman and FTIR spectroscopic study on the formation of the isomers MIL-68 (Al) and MIL-53 (Al), RSC Advances, 10 (2020) 7336-7348.
[39] T. Diao, P. White, I. Guzei, S.S. Stahl, Characterization of DMSO coordination to palladium (II) in solution and insights into the aerobic oxidation catalyst, Pd (DMSO) 2 (TFA) 2, Inorganic chemistry, 51 (2012) 11898-11909.
[40] M. Almáši, V. Zeleňák, P. Palotai, E. Beňová, A. Zeleňáková, Metal-organic framework MIL-101 (Fe)-NH_2 functionalized with different long-chain polyamines as drug delivery system, Inorganic Chemistry Communications, 93 (2018) 115-120.
[41] X. Hu, H. Hu, C. Li, T. Li, X. Lou, Q. Chen, B. Hu, Cobalt-based metal organic framework with superior lithium anodic performance, Journal of Solid State Chemistry, 242 (2016) 71-76.

[42] J.-S. Li, S.-L. Li, Y.-J. Tang, K. Li, L. Zhou, N. Kong, Y.-Q. Lan, J.-C. Bao, Z.-H. Dai, Heteroatoms ternary-doped porous carbons derived from MOFs as metal-free electrocatalysts for oxygen reduction reaction, Scientific reports, 4 (2014) 1-8.
[43] A.A. Razzaq, Y. Yao, R. Shah, P. Qi, L. Miao, M. Chen, X. Zhao, Y. Peng, Z. Deng, High-performance lithium sulfur batteries enabled by a synergy between sulfur and carbon nanotubes, Energy Storage Materials, 16 (2019) 194-202.
[44] J. Deng, P. Ren, D. Deng, L. Yu, F. Yang, X. Bao, Highly active and durable non-precious-metal catalysts encapsulated in carbon nanotubes for hydrogen evolution reaction, Energy & Environmental Science, 7 (2014) 1919-1923.